



A practical-oriented NiFe-based water-oxidation catalyst enabled by ambient redox and hydrolysis co-precipitation strategy

Wenxin Zhu^a, Tianshu Zhang^a, Yi Zhang^a, Zhihao Yue^a, Ying Li^a, Rong Wang^a, Yanwei Ji^a, Xuping Sun^{b,*}, Jianlong Wang^{a,*}

^a College of Food Science and Engineering, Northwest A&F University, Yangling 712100, Shaanxi, China

^b Institute of Fundamental and Frontier Science, University of Electronic Science and Technology of China, Chengdu 610054, Sichuan, China

ARTICLE INFO

Keywords:

Room temperature
Redox and hydrolysis co-precipitation
Ultralow-cost and scalable production
Nickel-iron hydroxide nanoarrays
Water oxidation

ABSTRACT

Although NiFe-based (oxy)hydroxides have been recognized as the most promising anode materials for industrial water splitting, the existed synthetic methods are difficult to fabricate NiFe-based (oxy)hydroxides simultaneously fulfilling the requirements of low-cost and ambient synthetic process, high performance, and easier realization of large-scale production. In this work, a simple while effective strategy was proposed to fabricate well-aligned Ni-Fe hydroxide nanosheets array on Ni foam (NiFe-OH NS/NF) by the ambient spontaneous redox reaction between Ni foam and Fe^{3+} and accompanied hydrolysis co-deposition of the generated Ni^{2+} , $\text{Fe}^{2+}/\text{Fe}^{3+}$, and OH^- . The tailored highly-oriented amorphous and nanoporous nanosheets structure as well as the strong electronic interaction between Ni and Fe species endow this NiFe-OH NS/NF with excellent OER activity that a large current density of 500 mA cm^{-2} could be well afforded at a low overpotential of 292 mV. Importantly, the manufacturing and raw-materials cost to synthesize the NiFe-OH NS/NF by this strategy is estimated to be just \$0.0165 per cm^2 , much lower than those for other reported self-supported Fe-containing catalyst materials. Also, this ambient means not only could be applicable to the large-scale production of size-tunable NiFe-OH NS/NF with stable nanoarray structure, but also could be easily used for the synthesis of NiCo NS/NF and NiCoFe NS/NF for applications.

1. Introduction

The global energy issues and subsequently serious environmental impacts related to the overexploitation of dwindling fossil fuels have stimulated research activities nowadays in the development of clean and sustainable energies [1,2]. Molecular hydrogen, due to its high energy density and carbon-free characteristic, is always believed to be a promising substitutable energy carrier for carbon-based fossil fuels in the future [3]. Among various approaches to hydrogen production, water electrolysis in alkali electrolyzer driven by renewable and intermittent energy resources like solar, wind and hydro powers has received much attention over the last decades [4,5], owing to the high-purity nature of generated hydrogen and sustainable/eco-friendly mode in which water is both the sole starting material and byproduct when clean energy is produced by converting hydrogen back to water [6,7]. At present, more and more reported works have focused on designing high-efficiency rechargeable Zn-air battery powered-water splitting tandem systems to generate pure hydrogen for the renewable energy industry [8–11], considering that both the rechargeable Zn-air battery

and water-splitting systems have the common necessary oxygen evolution reaction (OER) and this hybrid system is more feasible in the near future than aforementioned dispersive primary energy sources-driven water splitting ones. However, the OER process always involves sluggish kinetics from the multistep proton-coupled electron transfer ($4\text{OH}^- \rightarrow 2\text{H}_2\text{O} + \text{O}_2 + 4\text{e}^-$ in base) [7–13], deeply hindering the efficiencies of both water splitting and rechargeable Zn-air batteries. Thus, exploiting and designing highly-active catalyst materials to facilitate the OER is of great importance to reduce the substantial overpotential and thus make the whole process more energy-efficient. Noble metal-based oxides (e.g., IrO_2 and RuO_2) are regarded commonly as the benchmarking OER catalysts owing to their low Tafel slopes and overpotentials, particularly in base [7–13]. Nevertheless, the large-scale application of these materials is still limited by their scarcity, prohibitive cost and inferior durability [7–13]. To address this issue, tremendous efforts have been devoted to developing superior OER alternatives based on earth-abundant and non-precious metal elements, such as first-row transition metals [7,12–14].

Ni-based compounds have been proposed over the decades as good

* Corresponding authors.

E-mail addresses: xpsun@uestc.edu.cn (X. Sun), wanglong79@yahoo.com (J. Wang).

<https://doi.org/10.1016/j.apcatb.2018.12.021>

Received 18 August 2018; Received in revised form 30 November 2018; Accepted 6 December 2018

Available online 06 December 2018

0926-3373/© 2018 Elsevier B.V. All rights reserved.

candidates for OER due to their low cost, intrinsic high catalytic activity, and abundant reserves [15–17]. Further studies have revealed that the OER activities of these Ni-based catalysts could be further enhanced by the introduction of other transition metals like Fe, Co, Mo, and Zn into the Ni lattice sites [18–23]. With the abundant resource in the earth's crust, Fe attracts particular interest as a judicious choice in terms of its cost-effective and eco-friendly features [24] and the fact that just trace amounts of Fe could dramatically improve the OER activity of Ni-based (oxy)hydroxide [25]. In light of this, NiFe-based (oxy)hydroxides, as the benchmarking OER catalysts, thus have received much attention in water electrolysis and rechargeable metal- O_2 batteries [26–28]. Current researches on this kind of materials could be mainly divided into two aspects. One is to study the real active sites in Ni-Fe (oxy)hydroxides and the reason why the incorporation of Ni and Fe species could lead to an excellent OER performance [29–32]. Although the mechanism and real active sites in NiFe-based catalysts for OER remain highly controversial, there is consensus that the Fe dopants could deeply accelerate the charge-transfer kinetics and bring a synergistic effect between Ni sites and itself [25,33]. Another hot research aspect is focused on surface and interface engineering of these NiFe-based (oxy)hydroxides to enhance their OER catalytic activity and stability [19,28,34–40]. It should be noted here that more and more reported NiFe-based compounds yield remarkable OER performances close to the theoretical limit (1.23 V vs. RHE) with ultralow overpotentials (η of 180–230 mV to attain 10 mA cm^{-2}) and good stability, which means that the pursuit for the further improvement of their OER performance will soon encounter a bottleneck in the near future. Except for these two points, the raw-materials and manufacturing costs and synthetic process of NiFe-based (oxy)hydroxides should also be brought to the forefront for their large-scale utilization, which however have not caused enough concern. Minimizing the total production cost, simplifying the technological condition, and fabricating monolithic nanoarray architectures with more exposed active sites and no use of insulated polymer binders should be comprehensively considered to make NiFe-based anode materials more accessible to the scalable production for industrialized water electrolysis.

In this work, we propose an one-step room-temperature redox and accompanied hydrolysis co-precipitation strategy to in situ synthesize unique well-aligned Ni-Fe hydroxide nanosheets array on Ni foam (NiFe-OH NS/NF) for OER catalysis (Scheme 1). In this process, a redox reaction between Ni foam and Fe(III) occurs firstly, afterward, the co-precipitation of Fe(II), Fe(III) and Ni(II) occurs to generate uniform NiFe-OH nanosheets on the skeleton of Ni foam. Of note, this synthetic proposal just requires a piece of Ni foam and a certain amount of iron (III) nitrate nonahydrate with no use of other high-cost reagents and no additional external conditions like high temperature, high pressure or electric field. As expected, this NiFe-OH NS/NF anode exhibits a dramatically enhanced OER activity under harsh alkaline conditions. OER current densities of 50 and 500 mA cm^{-2} could be achieved at low

overpotentials of 244 and 292 mV, respectively, with a low Tafel slope of 46.7 mV dec^{-1} in 1.0 M KOH . The superb OER performance could be due to the improved catalytic activity and conductivity enabled by the synergism of Ni and Fe species in NiFe-OH nanosheets, the high utilization efficiency of catalytic active species and facilitated electrolyte penetration and O_2 diffusion enabled by the open-shelled NiFe-OH nanoarray structure and abundant nanopores within each NiFe-OH nanosheet, as well as the higher native activity enabled by the amorphous structure of NiFe-OH nanosheets. Besides, the estimated total cost per cm^2 of the NiFe-OH NS/NF is quite lower than those for other reported superior self-supported Fe-containing OER catalysts, and this strategy could also be applicable to the synthesis of NiFe-OH NS/NF at larger scales (e.g. $20 \times 18 \text{ cm}^2$), endowing this NiFe-OH NS/NF material with a higher likelihood of realizing industrialized production. Furthermore, overall water-splitting systems involved with a Ni_2P NS/NF cathode and this NiFe-OH NS/NF anode powered by the electrochemical analyzer and solar panel were constructed, in which a small cell voltage of 1.64 V was demanded to afford the overall current density of 10 mA cm^{-2} .

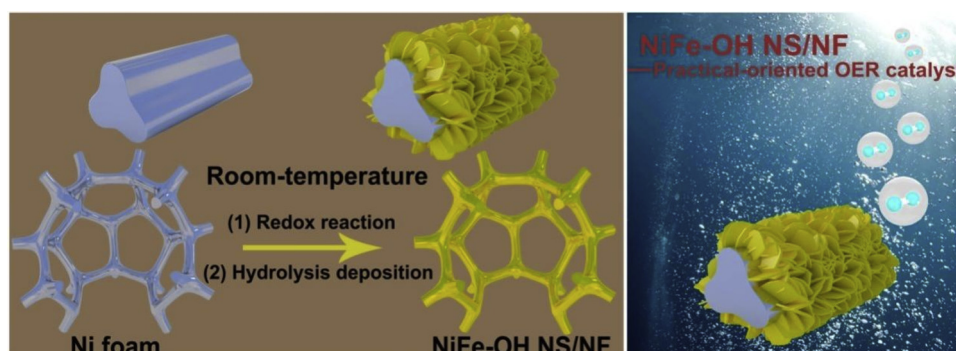
2. Experimental

2.1. Materials

Iron (III) nitrate nonahydrate [$\text{Fe}(\text{NO}_3)_3 \cdot 9\text{H}_2\text{O}$], Pt/C (10 wt% Pt) and $\text{RuCl}_3 \cdot x\text{H}_2\text{O}$ (35.0–42.0% Ru basis) were purchased from Aladdin Industrial Corporation (analytical grade). Hydrochloric acid (HCl, 36.0–38.0%), anhydrous ethanol ($\geq 99.7\%$), and potassium hydroxide (KOH) in this study were used as received without further purification. Ni foam (0.5 mm, areal density of 320 g cm^{-2}) was obtained from the Suzhou Jia Shi De Foam Metal Co. Ltd. The water used throughout all experiments was purified through a Millipore system.

2.2. Preparation of NiFe-OH NS/NF Electrode

NiFe-OH nanosheets were grown on Ni foam via room-temperature spontaneous redox and subsequent hydrolysis-deposition reactions. First, a piece of Ni foam ($2 \times 3 \text{ cm}^2$) was soaked in 3.0 M HCl for 5 min, then rinsed successively with high-purity ethanol and deionized water to remove the organic impurities and oxide layer on the surface prior to using as a substrate. Second, this pretreated Ni foam was transferred into a aqueous solution containing 100 mM of $\text{Fe}(\text{NO}_3)_3 \cdot 9\text{H}_2\text{O}$ for 7 h. Following this, NiFe-OH nanosheets array supported on Ni foam could be well obtained. The loading mass of NiFe-OH nanosheets on Ni foam was calculated to be $\sim 2.384 \text{ mg cm}^{-2}$ by use of the flame atomic absorption spectrometry (FAAS) analysis reported in a previous work. [41] The details on the calculation of loading mass of NiFe-OH nanosheets on Ni foam are shown in the Supplementary Information. The synthesis processes of NiCo NS/NF and NiCoFe NS/NF were similar to



Scheme 1. Schematic illustration of the preparation process of NiFe – OH NS/NF via the ambient redox and hydrolysis co-precipitation strategy and its application in practical-oriented water oxidation.

that for the NiFe-OH NS/NF, in which the 100 mM Fe^{3+} should be substituted to 100 mM Co^{2+} and 100 mM $\text{Fe}^{3+} + 100 \text{ mM } \text{Co}^{2+}$, respectively.

2.3. Preparation of Ni_2P NS/NF Electrode

First, Ni foam was soaked in 3.0 M HCl solution and then rinsed with ethanol and DI water. Second, in a typical synthesis, 4 mmol Ni $(\text{NO}_3)_2 \cdot 6\text{H}_2\text{O}$, 20 mmol Urea, and 8 mmol NH_4F were mixed together in 40 ml deionized (DI) water, then stirred for several minutes to form a clear solution. This solution and a piece of Ni foam ($2 \times 3 \text{ cm}^2$) were transferred into a 50 ml Teflon-lined stainless-steel autoclave, then sealed and maintained at 120°C for 6 h. After that, the sample was taken out, washed with DI water and dried in a vacuum oven at 80°C to obtain the $\text{Ni}(\text{OH})_2$ NS/NF. Afterwards, the $\text{Ni}(\text{OH})_2$ NS/NF and 300 mg of $\text{NaH}_2\text{P}_2\text{O}_7$ were placed at the downstream side and upstream side of the furnace, respectively. Subsequently, this sample was heated at 300°C for 2 h with a heating speed of 2°C min^{-1} in Ar atmosphere. After that, Ni_2P NS/NF could be obtained. The loading mass of Ni_2P nanosheets on Ni foam was calculated to be $\sim 4.62 \text{ mg cm}^{-2}$.

2.4. Preparation of RuO_2 /NF and Pt/C/NF electrodes

RuO_2 powder was synthesized according to previously reported works. 2.61 g $\text{RuCl}_3 \cdot x\text{H}_2\text{O}$ was dissolved in 100 ml deionized water and heated at 100°C for 10 min under air atmosphere, followed by the addition of 10 ml 1.0 M KOH. The mixture was then stirred for another 45 min at this temperature. After reaction, the solution was centrifuged for 15 min and then the precipitate could be obtained. After that, the precipitate was washed with water for four times, totally dried at 70°C , and finally calcined at 500°C in air for 1 h to obtain the RuO_2 powder. Next, certain amounts of Pt/C and RuO_2 powders were dispersed respectively in a 2 ml 25:24:1 water/ethanol/Nafion (5 wt%) solution to form their inks. Then, according to the loading masses of NiFe-OH NS/NF and Ni_2P NS/NF, the inks were drop-casted on the surface of a $0.5 \times 0.5 \text{ cm}^2$ Ni foam to form the RuO_2 /NF and Pt/C/NF electrodes.

2.5. Physical characterizations

Scanning electron microscope (SEM) images, energy-dispersive X-ray spectrometry (EDX) and corresponding elemental mappings data of the NiFe-OH NS/NF were obtained on a Hitachi S-4800 microscope at accelerating voltages of 10 and 20 kV. The transmission electron microscopy (TEM), high-resolution TEM (HRTEM), and selected-area electron diffraction (SAED) images were acquired on a Hitachi H-8100 electron microscopy (Hitachi, Tokyo, Japan) with an accelerating voltage of 200 kV. The amorphous structure of NiFe-OH NS/NF was analyzed by a Bruker D8 Advanced Diffractometer System with a Cu K α (1.5418 \AA) source (40 kV, 40 mA) in transmission mode over the θ range of $5\text{--}100^\circ$. X-ray photoelectron spectroscopy (XPS) test was performed on an ESCALABMK II X-ray photoelectron spectrometer using Mg as the exciting source to determine the chemical compositions and valence states in the NiFe-OH nanosheets. Flame atomic absorption spectrometry (FAAS, Z-2000, Hitachi) was used for the determination of the content of dissolved Ni residue in the synthesis process. The sessile drop method was applied to measure the water contact angle under $\sim 30\%$ humidity using a contact angle instrument (JY-PHa, Chengde).

2.6. Electrochemical characterizations

Electrochemical measurements were performed with a CHI660E electrochemical workstation (CH Instruments, Inc., Shanghai) in a standard three-electrode system at room temperature (25°C), wherein the as-prepared NiFe-OH NS/NF was used as the working electrode, and a graphite plate and a mercuric oxide electrode (MOE) were used as the

counter electrode and reference electrode, respectively. The measurements were carried out in 1.0 M KOH and the geometric area of working electrode was controlled as 0.25 cm^2 in each test. Polarization curves were recorded by linear sweep voltammetry with a small scan rate of 5 mV s^{-1} to minimize the capacitive current. Electrochemical impedance spectroscopy (EIS) measurements were conducted at an anodic polarization potential of 0.55 V vs. MOE in a frequency range from 100 kHz to 0.0005 Hz by applying an AC voltage of 5 mV. Tafel plots were fitted to the Tafel equation ($\eta = b \log j + a$, where η is the overpotential, j is the current density, and b is the Tafel slope) and retained in their linear portions at low overpotentials. For parallel comparison with literature values, all the measured potentials referred to reversible hydrogen electrode (RHE) were converted by the following equation: $E(\text{RHE}) = E(\text{MOE}) + 0.9254$ (1.0 M KOH). The long-term durability test was performed by chronopotentiometric measurements. All currents presented were corrected against ohmic potential drop. The overall water-electrolysis systems driven by the electrochemical workstation and another power supply pattern of 2.0 V solar panel were also established with NiFe-OH NS/NF as the anode and Ni_2P NS/NF as the cathode in a two-electrode setup (1.0 M KOH).

3. Results and discussion

3.1. Morphology and structural characterization of the NiFe-OH-OH NS/NF

The fabrication process of NiFe-OH NS/NF is illustrated in Fig. 1a and relevant experimental details are shown in the Supporting Information. An obvious change of optical characteristic from silvery grey to dark yellow could be observed after room-temperature redox and hydrolysis-deposition reactions induced by Fe^{3+} , initially proving that the NiFe-phase was *in situ* formed on Ni foam. The morphology and composition of this NiFe-OH NS/NF was further confirmed by some physical characterizations like X-ray diffraction (XRD), scanning electron microscopy (SEM), transmission electron microscopy (TEM), and X-ray photoelectron spectroscopy (XPS). No significant differences of the diffraction peaks exist in the XRD patterns of bare Ni foam and NiFe-OH NS/NF, indicative of the amorphous or low-crystallinity structure of the generated NiFe-OH phase (Fig. 1b). Three diffraction peaks located at $\approx 44.5^\circ$, 51.8° , and 76.4° could be ascribed to the (111), (200), and (220) planes of Ni (JCPDS no. 65-2865) [42].

The surface morphology of this as-obtained NiFe-OH NS/NF was then investigated by SEM and TEM analyses. As exhibited in Fig. 1c and S1, highly uniform and compact NiFe-OH nanosheets grow vertically upon the entire smooth surface of Ni foam and consequently form a lamellar structure with a thickness of about $1.43 \mu\text{m}$ (cross-sectional SEM image in the inset). The high-resolution SEM image in Fig. 1d shows that the dense and open-shelled nanosheets are intersected to form a tridimensional network, wherein each unit has a lateral size of hundreds of nanometres and thickness of $\sim 24 \text{ nm}$ (closer view of these nanosheets in the inset). Note that, these NiFe-OH nanosheets also have rough surface and large space among adjacent layers, which might be beneficial to the increase of active surface area and penetration/diffusion of electrolyte and generated O_2 . Energy-dispersive X-ray (EDX) spectrum and elemental mappings (Fig. 1e) confirm the presence and homogeneous distribution of Ni, Fe, and O elements on the surface of NiFe-OH NS/NF. Low-resolution TEM image of an individual NiFe-OH layer scratched from Ni foam also shows a well-defined nanosheet topology (inset of Fig. 1f). A nanoporous structure could be distinctly observed from the closer view of the edge of the NiFe-OH nanosheet (Fig. 1f). The corresponding high-resolution TEM (HRTEM) image (Fig. 1g) presents the homogeneous amorphous structure with no perceptible lattice fringes of NiFe-OH nanosheets, consistent well with the above-mentioned XRD result. This result could be further confirmed by the selected-area electron diffraction (SAED) pattern taken from an area including several NiFe-OH nanosheets that barely perceptible

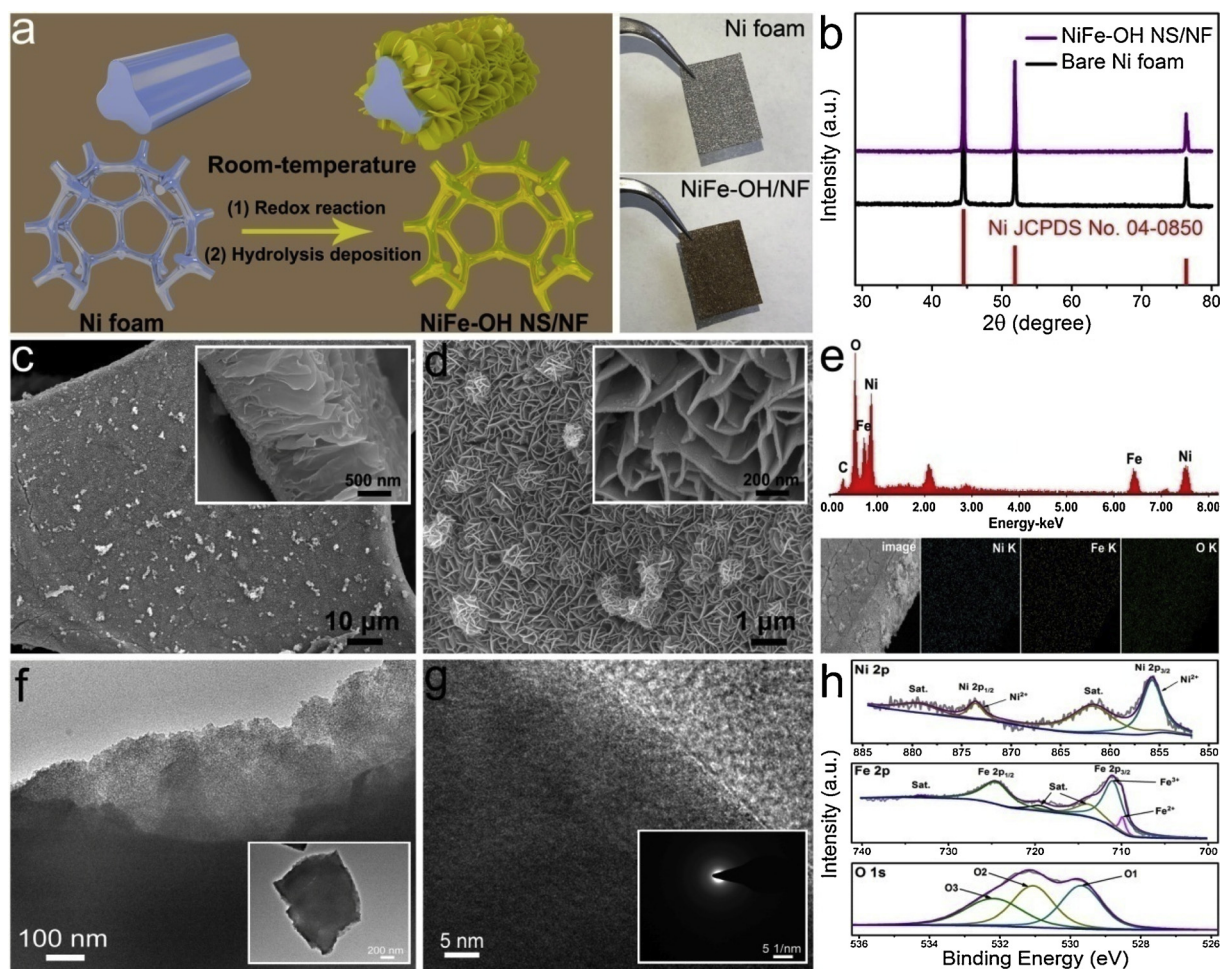


Fig. 1. Physical characterization of the NiFe-OH NS/NF. (a) Schematic diagram of the synthetic process of NiFe-OH NS/NF and comparison of photographs of bare Ni foam and NiFe-OH NS/NF. (b) XRD patterns of NiFe-OH NS/NF and bare Ni foam. (c) Low-magnification SEM image of NiFe-OH NS/NF (inset: the cross-sectional SEM image of the NiFe-OH NS/NF). (d) High-magnification SEM image of NiFe-OH NS/NF (inset: closer view of these nanosheets). (e) Energy-dispersive X-ray (EDX) spectrum and elemental mapping images of the NiFe-OH NS/NF. (f) Low-resolution TEM images of scratched individual NiFe-OH nanosheet from Ni foam. (g) High-resolution TEM image of a randomly-selected spot on this NiFe-OH nanosheet (inset: SAED pattern taken from an area including several NiFe-OH nanosheets). (h) The high-resolution XPS spectra in the regions of Ni 2p, Fe 2p, and O 1s for NiFe-OH NS/NF.

diffraction rings could be observed (inset of Fig. 1g). Here, the nanoporous structure offers the NiFe-OH nanosheets high specific surface area, efficient exposure of catalytic active sites, fast electrolyte penetration/diffusion, and free diffusion of O_2 [43,44], while the amorphous structure endows these NiFe-OH nanosheets with large surface area, high conductivity, and thus high OER activity [34,45–48]. Besides, the surface hydrophilicity/hydrophobicity states of the untreated Ni foam, pretreated Ni foam and the as-synthesized NiFe-OH NS/NF were also recorded (Fig. S2). These results demonstrate the good hydrophilicity of the NiFe-OH NS/NF. The flexural property of the NiFe-OH NS/NF was further tested by deforming this electrode under various bending states. The optical and SEM images in Fig. S3 indicate this electrode has a good mechanical flexibility with robust NiFe-OH nanoarray structures.

Elemental composition and corresponding chemical states of the outer surface of NiFe-OH NS/NF were elucidated by XPS analysis. The XPS survey scan again corroborates the co-existence of Ni, Fe, and O elements on the surface of NiFe-OH NS/NF (Fig. S4). Fig. 1h clearly exhibits the high-resolution XPS spectra in the regions of Ni 2p, Fe 2p, and O 1s. In the Ni 2p spectrum, binding energies of Ni 2p_{1/2} and Ni 2p_{3/2} located at 855.7 and 873.8 eV were assigned to Ni²⁺, accompanied by two prominent shakeup satellite peaks (861.8 and 879.5 eV) [49–51]. The Fe 2p spectrum features with two prominent peaks at binding energies of 711.1 and 724.7 eV, corresponding to Fe 2p_{3/2} and Fe 2p_{1/2}, respectively. The deconvoluted Fe 2p_{3/2} signals appeared at

709.9 and 711.1 eV could be well ascribed to the Fe²⁺ and Fe³⁺ species in the sample [51,52]. Additionally, the high-resolution O 1s region is comprised of three distinct characteristic peaks typical of metal-oxygen bonds (O1, 529.7 eV) [50,51], a high number of defect sites with low oxygen coordination within the oxide crystal, adsorbed oxygen, or hydroxide species at the surface (O2, 531.1 eV) [49,54], and the multiplicity of physically and chemically absorbed water at or near the surface of NiFe-OH NS/NF (O3, 532.2 eV) [53]. All these results evidently prove the consubstantial growth of amorphous and nanoporous Ni-Fe hydroxide nanosheets array on Ni scaffold by the spontaneous room-temperature redox and hydrolysis-deposition process.

Besides, the SEM images of NiFe-OH NS/NF synthesized with different concentrations of Fe³⁺ were also recorded (Fig. S5). Obviously, with the increase of Fe³⁺ concentration (< 200 mM), the upright NiFe-OH nanosheets gradually emerged on the Ni foam. When the concentration of Fe³⁺ exceeded 100 or 200 mM, the nanosheets topology began to degenerate, and when the concentration ultimately reached to 500 mM, the NiFe-OH nanosheets array structure was totally replaced with corresponding film, likely due to the excessive reaction of Ni foam with Fe³⁺. It is worth emphasizing that when the reaction time exceeds 7 h or the Fe³⁺ concentration exceeds 300 mM, the mechanical strength of this monolithic NiFe-OH NS/NF will dramatically decrease, bringing a fragile electrode and decreased OER performance.

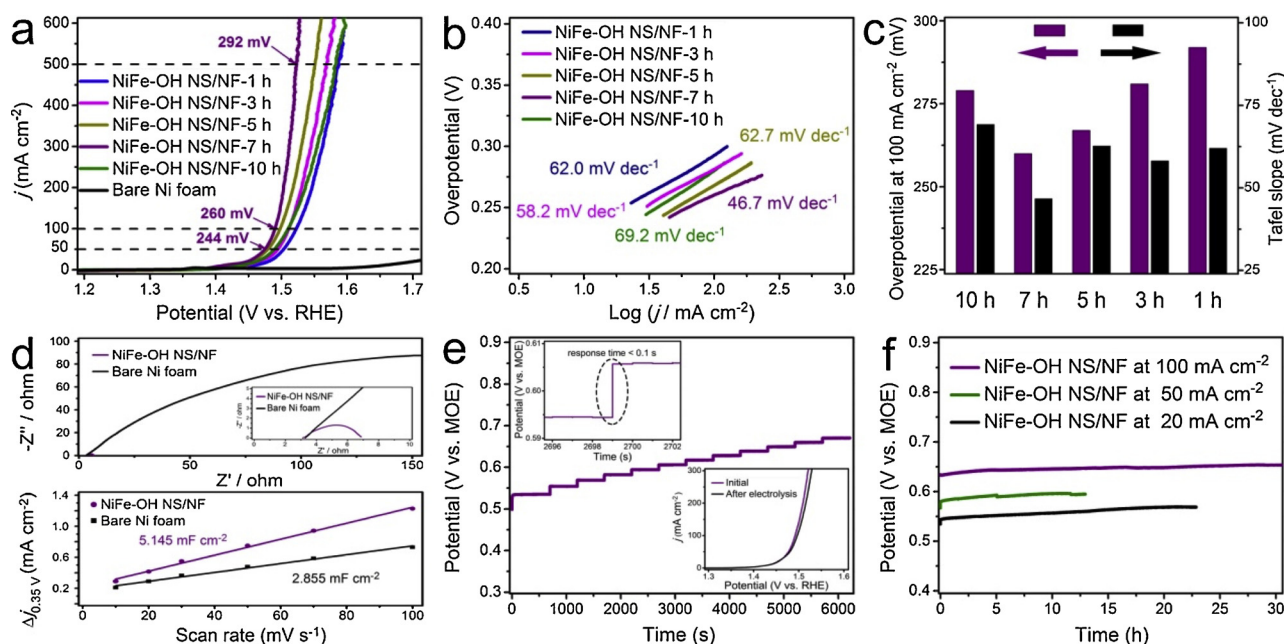


Fig. 2. Electrochemical characterization. (a) OER polarization curves of different NiFe-OH NS/NF anodes synthesized in 100 mM Fe^{3+} -containing aqueous solution with soaking times from 1 to 10 h in 1.0 M KOH at a scan rate of 5 mV s^{-1} . (b) Corresponding Tafel plots derived from the curves in a. (c) Comparisons on the overpotential at 100 mA cm^{-2} and Tafel slope of different NiFe-OH NS/NF anodes with soaking times from 1 to 10 h. (d) The Nyquist plots and capacitive current density (Δj) at 0.35 V (vs. MOE) as a function of scan rate in the range of 0.3–0.4 V for NiFe-OH NS/NF and bare Ni foam in 1.0 M KOH. (e) The multi-step chronopotentiometric curve of NiFe-OH NS/NF recorded in 1.0 M KOH with anodic current densities increasing from 10 to 120 mA cm^{-2} (insets: response time and LSV curves before and after electrolysis). (f) Chronopotentiometric curves for NiFe-OH NS/NF recorded at constant current densities of 20, 50, and 100 mA cm^{-2} .

3.2. Evaluation of electrocatalytic water-oxidation activity of the NiFe–OH NS/NF

The electrocatalytic OER performance of NiFe-OH NS/NF was evaluated in a typical three-electrode system in 1.0 M KOH with NiFe-OH NS/NF as the working electrode, graphite rod as the counter electrode and Hg/HgO as the reference electrode. For comparison, the OER polarization curves of bare Ni foam and RuO_2/NF was also recorded under the same condition. The iR -corrected OER polarization curves of NiFe-OH NS/NF with different soaking time and bare Ni foam were recorded in Fig. 2a. Obviously, Ni foam shows negligible OER response, while the OER activities of the as-prepared series of NiFe-OH NS/NF render much lower onset potentials and higher current densities, indicating that the coupling of Ni and Fe species could significantly enhance the electrocatalytic OER activity. The NiFe-OH NS/NF immersed for seven hours exhibits the best catalytic activity with low overpotentials of only 244 and 292 mV to reach current densities of 50 and 500 mA cm^{-2} , respectively, even superior to those for the RuO_2/NF (Fig. S6) and most of reported advanced Fe-containing anodes (Table 1 and S1). Apparently, this anode could satisfy well the criteria of commercial water electrolyzers that OER current densities above 500 mA cm^{-2} should be delivered at low overpotentials ($< 300 \text{ mV}$) [7,34].

The Tafel plots of NiFe-OH NS/NF with different soaking time were shown in Fig. 2b. The linear portions of Tafel plots are fitted to the Tafel equation: $\eta = b \log j + a$, wherein j is the current density, b is the Tafel slope, and a is the intercept relative to the exchange current density j_0 [55]. The NiFe-OH NS/NF fabricated under the optimal condition has the lowest OER Tafel slope of 46.7 mV dec^{-1} , revealing a more favorable OER kinetics. More clear comparisons on the overpotential at 100 mA cm^{-2} and Tafel slope of NiFe-OH NS/NF anodes with different soaking time were shown in Fig. 2c. Here, the excellent OER performance could be mainly attributed to the synergistic effect enabled by the incorporation of Fe species, the amorphous nature of NiFe-OH nanosheets, and the unique nanoarray structure with abundant nanopores.

The improved conductivity induced by the incorporation of Fe was

verified by recording the electrochemical impedance spectroscopy (EIS) data of bare Ni foam and NiFe-OH NS/NF. Fig. 2d shows the representative Nyquist plots of bare Ni foam and NiFe-OH NS/NF, wherein the diameter of the arc decreases seriously after reaction, indicative of a dramatically improved charge-transfer kinetics of NiFe-OH NS/NF [33,56]. Besides, we initially assumed that the improvement of OER performance is also related to the increase of electrochemical surface area (ECSA). Normally, cyclic voltammetry (CV) measurement is always used for calculating the ECSA, since the capacitive currents associated with electrical double-layer charging are considered to be able to quantify the accessible surface area between active sites and electrolyte [57]. The capacitive current density (Δj) at 0.35 V (vs. MOE) as a function of scan rate for NiFe-OH NS/NF and Ni foam (Fig. 2d) derived from corresponding typical cyclic voltammograms (Fig. S7) show that the double-layer capacitances (C_{dl}) of Ni foam and NiFe-OH NS/NF are 2.855 and 5.145 mF cm^{-2} , respectively. Considering the C_{dl} value is positively correlative with that of ECSA [58], a conclusion that the ECSA of NiFe-OH NS/NF is about 1.8 times larger than that for bare Ni foam could be obtained, which might be ascribed to the derived well-aligned nanoporous and amorphous nanosheets structure. In a word, the improved conductivity and enlarged active surface area become the direct key factors in the improved OER property of NiFe-OH NS/NF.

Multi-current chronopotentiometry curve of the NiFe-OH NS/NF anode was also recorded in 1.0 M KOH with the anodic current densities increasing from 10 to 120 mA cm^{-2} and an increment of 10 mA cm^{-2} per step (Fig. 2e). The potential immediately levels off at 10 mA cm^{-2} and remains constant for the rest 500 s, while other steps also keep constant and respond quickly to another one (less than 0.1 s), illustrating that the NiFe-OH NS/NF has excellent mass transportation, conductivity and mechanical robustness toward OER catalysis [43]. The polarization curve after electrolysis only exhibits slight degradation compared with the initial one, suggesting the good stability of this electrode working in base (inset in Fig. 2e). What's more, the long-term durability test of this NiFe-OH NS/NF toward OER was performed in 1.0 M KOH at several fixed current densities of 20, 50, and 100 mA cm^{-2} .

Table 1

Comparison of the cost and catalytic performance for this NiFe-OH NS/NF with reported superior self-supported Fe-containing OER electrocatalysts.

| Electrocatalyst | Used substrates and chemicals | Amount used (cm ² or mg or mmol) | Unit cost (US \$ per cm ² or g or mL) | Cost (US \$) | Total cost (US \$ per cm ² of catalyst) | Other cost-increasing factors | η_{50} (mA cm ⁻² (mV)) | Ref. |
|--|--|---|--|--------------|--|--|--|---|
| NiFe-MOF/NF | nickel foam | 2 cm ² | 0.00568 | 0.0114 | 0.0542 | Sealed for reaction at 60 °C for 20 h | / | <i>Nat. Commun.</i> 2017 , 8, 15341 |
| | Ni(Ac) ₂ ·4H ₂ O | 8 mg | 0.613 | 0.00491 | | | | |
| | Fe(NO ₃) ₃ ·9H ₂ O | 2 mg | 0.0321 | N/A | | | | |
| | 2,6-naphthalenedicarboxylate | 10 mg | 9.223 | 0.0922 | | | | |
| S-NiFe ₂ O ₄ /NF | nickel foam | 4 cm ² | 0.00568 | 0.0227 | 0.213 | Electrodeposition at -1.1 V for 600 s; CVD at 250 °C for 2 h | 291 | <i>Nano Energy</i> 2017 , 40, 264–273 |
| | Ni(NO ₃) ₂ ·6H ₂ O | 0.1 mmol | 4.776 | 0.139 | | | | |
| | Fe(NO ₃) ₃ ·9H ₂ O | 0.2 mmol | 0.0321 | 0.00259 | | | | |
| | thiourea | 6 mmol | 1.508 | 0.689 | | | | |
| Fe _{11%} -NiO/NF | nickel foam | 4 cm ² | 0.00568 | 0.0227 | 1.048 | Hydrothermal deposition at 120 °C for 8 h; CVD at 350 °C for 2 h | 259 | <i>J. Catal.</i> 2018 , 358, 243–252 |
| | Ni(NO ₃) ₂ ·6H ₂ O | 3 mmol | 4.776 | 4.166 | | | | |
| | FeCl ₃ ·6H ₂ O | 0.4 mmol | 0.0321 | 0.00347 | | | | |
| | urea | 5 mmol | 0.0255 | 0.00766 | | | | |
| NiFeV LDHs/NF | nickel foam | 12 cm ² | 0.00568 | 0.0682 | 0.490 | Hydrothermal deposition at 120 °C for 12 h | / | <i>Adv. Energy Mater.</i> 2018 , 8, 1703341 |
| | Ni(NO ₃) ₂ ·6H ₂ O | 2.4 mmol | 4.776 | 3.333 | | | | |
| | Fe(NO ₃) ₃ ·9H ₂ O | 0.4 mmol | 0.0321 | 0.00519 | | | | |
| | urea | 5 mmol | 0.0255 | 0.00766 | | | | |
| S-NiCoFe LDH/CC | VCl ₃ | 0.4 mmol | 39.167 | 2.464 | | Hydrothermal deposition at 120 °C for 14 h; Dry at 80 °C for 24 h under vacuum | 241 | <i>J. Mater. Chem. A</i> 2018 , 6, 3224–3230 |
| | carbon cloth | 4 cm ² | 0.0474 | 0.190 | 0.398 | | | |
| | Co(NO ₃) ₂ ·6H ₂ O | 1 mmol | 1.072 | 0.312 | | | | |
| | urea | 11 mmol | 0.0255 | 0.0169 | | | | |
| NiFeRu-LDH/NF | Ni(NO ₃) ₂ ·6H ₂ O | 0.75 mmol | 4.776 | 1.0416 | | Hydrothermal deposition at 120 °C for 12 h | 248 | <i>Adv. Mater.</i> 2018 , 30, 1706279 |
| | Fe(NO ₃) ₃ ·9H ₂ O | 0.25 mmol | 0.0321 | 0.00324 | | | | |
| | Na ₂ S·9H ₂ O | 90 mg | 0.299 | 0.0269 | | | | |
| | nickel foam | 3 cm ² | 0.00568 | 0.0170 | 0.688 | | | |
| MoFe:Ni(OH) ₂ /NiOOH/NF | Ni(NO ₃) ₂ ·6H ₂ O | 0.3 mmol | 4.776 | 0.417 | | Hydrothermal deposition at 150 °C for 24 h; electrochemical oxidation at 1.6 V for 1 h | 276 | <i>ACS Catal.</i> 2018 , 8, 2359 – 2363 |
| | Fe(NO ₃) ₃ ·9H ₂ O | 0.24 mmol | 0.0321 | 0.00310 | | | | |
| | RuCl ₃ ·xH ₂ O | 0.06 mmol | 130.430 | 1.623 | | | | |
| | urea | 2 mmol | 0.0255 | 0.00300 | | | | |
| Cu@CoFe LDH/CF | nickel foam | 8 cm ² | 0.00568 | 0.0454 | 0.0723 | CVD at 180 °C for 1 h; Electrochemical reduction at -0.4 V; Electrodeposition at -1.0 V for 60 s | 276 | <i>Nano Energy</i> 2017 , 41, 327–336 |
| | urea | 50 mg | 0.0255 | 0.00128 | | | | |
| | NiCl ₂ ·6H ₂ O | 50 mg | 8.092 | 0.405 | | | | |
| | FeCl ₃ ·6H ₂ O | 3 mg | 0.0321 | N/A | | | | |
| Cu@NiFe LDH/CF | (NH ₄) ₆ Mo ₇ O ₂₄ ·4H ₂ O | 25 mg | 5.062 | 0.127 | | CVD at 180 °C for 1 h; Electrochemical reduction at -0.4 V; Electrodeposition at -1.0 V for 90 s | 245 | <i>Energy Environ. Sci.</i> 2017 , 10, 1820–1827 |
| | copper foam | 10 cm ² | 0.0134 | 0.134 | 0.620 | | | |
| | (NH ₄) ₂ S ₂ O ₈ | 10 mmol | 0.569 | 1.298 | | | | |
| | Co(NO ₃) ₂ ·6H ₂ O | 15 mmol | 1.072 | 4.680 | | | | |
| NiFeO _x /IF | FeSO ₄ ·7H ₂ O | 15 mmol | 0.0214 | 0.0892 | | / | / | <i>Adv. Energy Mater.</i> 2017 , 7, 1700107 |
| | copper foam | 10 cm ² | 0.0134 | 0.134 | 2.235 | | | |
| | (NH ₄) ₂ S ₂ O ₈ | 10 mmol | 0.569 | 1.298 | | | | |
| | Ni(NO ₃) ₂ ·6H ₂ O | 15 mmol | 4.776 | 20.832 | | | | |
| NiFe-OH/NF | FeSO ₄ ·7H ₂ O | 15 mmol | 0.0214 | 0.0892 | | / | 244 | This work |
| | iron foam | 2.5 cm ² | 0.0189 | 0.0473 | 0.0729 | | | |
| | NiSO ₄ ·6H ₂ O | 1 mmol | 0.515 | 0.135 | | / | | |
| | nickel foam | 6 cm ² | 0.00568 | 0.0341 | 0.0165 | | | |
| | Fe(NO ₃) ₃ ·9H ₂ O | 5 mmol | 0.0321 | 0.0648 | | | | |

Note: Some details on this table are shown in the Supplementary Material.

². It could be seen that all the operating potentials under different current densities almost keep stable (Fig. 2f).

3.3. Physical characterization of the NiFe-OH NS/NF after OER Catalysis

To further clarify the structural and compositional stability of this material during OER electrolysis, physical characterizations of the NiFe-OH NS/NF after long-term electrolysis at 20 mA cm⁻² for 12 h were employed. As shown in Fig. 3a, the XRD patterns of NiFe-OH NS/NF after electrolysis recorded for two times were almost unchanged compared with that for the initial one, proving that the NiFe-OH nanosheets were still in the amorphous form. Besides, the layered structure composed of uniform NiFe-OH nanosheets was basically preserved with a rougher surface on the surface of Ni foam (Fig. 3b and c). TEM and HRTEM images (Fig. 3d) also demonstrate the NiFe-OH nanosheets retained well the analogously amorphous and laminar structure after OER catalysis. The high-resolution Ni 2p XPS spectrum (Fig. 3e) indicates that Ni³⁺ generated on the surface of catalyst after electrolysis, while the high-resolution Fe 2p spectrum (Fig. 3f) shows there is almost

no differences in the valence states of Fe element in the NiFe-OH NS/NF before and after OER catalysis. The mixed-valence Ni²⁺/Ni³⁺ and Fe²⁺/Fe³⁺ species with rich reversible redox behaviors might also be responsible for the high OER activity of this catalyst. These results indicate this NiFe-OH NS/NF has acceptable durability in the OER process.

3.4. Growth mechanism and explanation for the OER activity of the NiFe-OH NS/NF

Based on the above experimental results, we could deduce a reasonable growth mechanism of NiFe-OH nanosheets array on Ni foam: (i) a redox reaction between Ni foam and Fe³⁺ occurs and simultaneously a mass of Fe²⁺ and Ni²⁺ are produced near the surface of Ni foam (Eq. 1); (ii) partial Fe²⁺ is gradually oxidized into Fe³⁺ associated with OH⁻ based on the oxidation-reduction reaction under the action of water and oxygen (Eq. 2); (iii) via the co-precipitation of Fe²⁺, Fe³⁺, and Ni²⁺, the highly uniform NiFe-OH nanosheets supported on Ni foam could be definitively achieved (Eq. 3). Meanwhile, the excellent OER

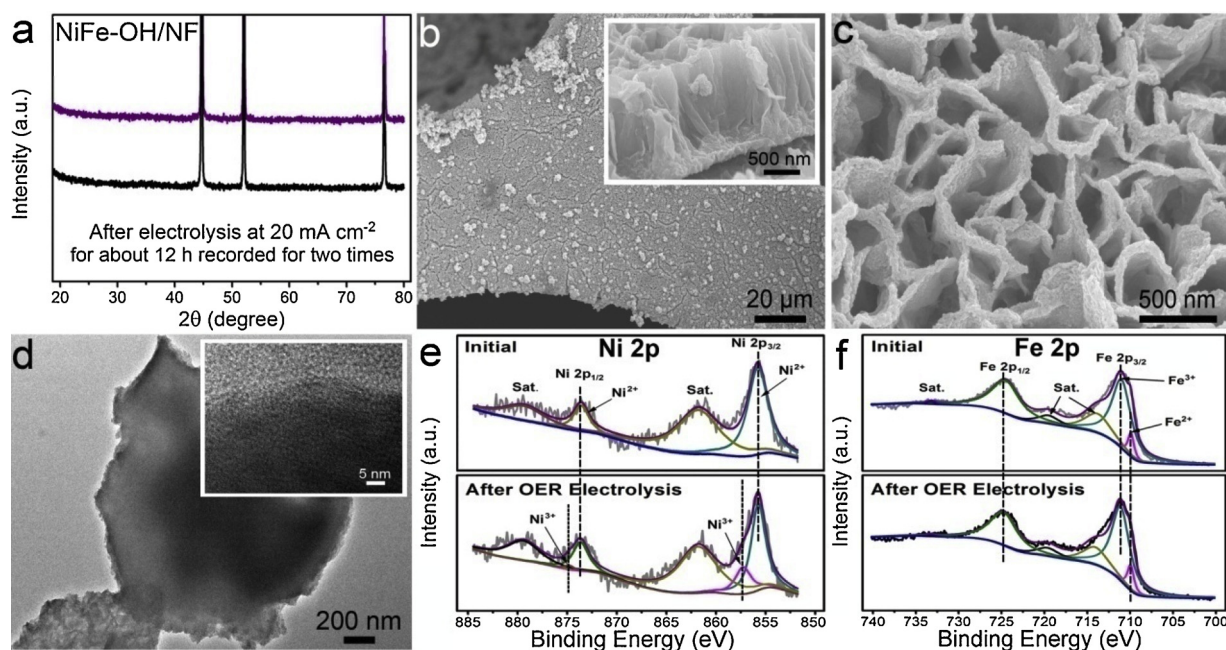
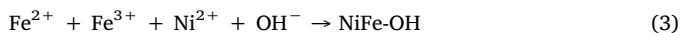
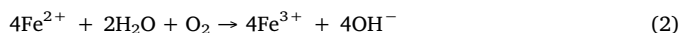


Fig. 3. Physical characterization of the NiFe-OH NS/NF after OER electrolysis. (a) XRD patterns of NiFe-OH NS/NF after OER electrolysis at 20 mA cm⁻² for 12 h recorded for two times. (b) Low-magnification SEM image of NiFe-OH NS/NF after OER catalysis (inset: cross-sectional SEM image of NiFe-OH NS/NF after electrolysis). (c) High-magnification SEM image of NiFe-OH NS/NF after OER catalysis. (d) Low-resolution TEM image of scratched NiFe-OH nanosheets from Ni foam after OER electrolysis (inset: corresponding high-resolution TEM image). The high-resolution XPS spectra in the regions of (e) Ni 2p and (f) Fe 2p recorded for NiFe-OH NS/NF before and after OER test.

performance of this integrated NiFe-OH NS/NF could be specifically put down to the following four aspects. First, the NiFe-OH phase is intrinsically active toward OER due to the synergy of Ni and Fe species and accelerated charge-transfer kinetics [25,33]; Second, the vertical NiFe-OH nanosheets array structure, large open space among the nanosheets, and abundant nanopores within each NiFe-OH nanosheet endow the high utilization efficiency of catalytic active species and facilitated electrolyte penetration and O₂ diffusion [34]; Third, the amorphous nature endows these NiFe-OH nanosheets with higher catalytic power [34,45]; Finally, this *in situ* growth mode enables strong adhesion of NiFe-OH nanosheets with Ni foam, which contributes to the good compositional and structural stability of this integrated electrode for OER.



3.5. Evaluation of the practicability and universality of this synthetic strategy

In addition to the OER performance, the cost and feasibility of large-scale production of this NiFe-OH NS/NF, as well as the universality of this synthetic strategy were also evaluated. In Table 1, the manufacturing and raw-materials cost of the NiFe-OH NS/NF is estimated to be just \$0.0165 per cm², much lower than those for other reported self-supported Fe-containing catalyst materials. Besides, the NiFe-OH NS/NF at scales from 1 cm² to 360 cm² could be easily obtained by this strategy with well-aligned nanosheets array morphology (Fig. 4). Also, this synthetic method was demonstrated to be able to extendable to the synthesis of NiCo NS/NF and NiCoFe NS/NF (Fig. S8). These results confirm this ambient synthetic strategy not only could be utilized for the low-cost and large-scale production of size-tunable NiFe-OH NS/NF with superior OER activity, but also could be easily used for the synthesis of other transition metal-containing nanoarrays on Ni foam

for applications.

3.6. Overall water splitting driven by the NiFe-OH NS/NF (+)||Ni₂P NS/NF (-) Pair

Moreover, given its superb OER activity and stability, this NiFe-OH NS/NF anode was subsequently integrated with a Ni foam-supported nickel phosphide nanosheets array (Ni₂P NS/NF) cathode to try to build a high-efficiency overall water splitting system. Ni₂P, owing to its high HER activity with low onset potential and large cathodic current response, has been deemed as a potential alternative to noble-metal based HER electrocatalysts [59]. Physical characterizations like XRD, SEM, EDX and elemental mappings demonstrate the successful synthesis of Ni₂P NS/NF (Fig. S9). The HER activity and stability of Ni₂P NS/NF in base were also confirmed. Fig. S10a indicates that compared with NiFe-OH NS/NF and Ni foam, the Ni₂P NS/NF has a much higher HER performance with a low overpotential of ~133 mV to achieve a cathodic current density of 10 mA cm⁻². And it could be seen that, though the HER performance of the Pt/C/NF is better than that for the Ni₂P NS/NF at low overpotentials, the rise of HER current density for the Ni₂P NS/NF is faster than that for the Pt/C/NF (Fig. S11), which could be explained to a great extent by the easier diffusion of electrolytes and generated O₂ enabled by the Ni₂P nanosheets array structure. Multi-current chronopotentiometry test manifests that the Ni₂P NS/NF could maintain stable potentials at various current densities (Fig. S10b) with only slight degradation reflected on the HER polarization curve after this process. All these results prove the Ni₂P NS/NF is a superior HER cathode. Then, the overall alkaline water-splitting device was built with the electrode pair of NiFe-OH NS/NF (+)||Ni₂P NS/NF (-) (Fig. 5a). This combined system just requires a small voltage of ~1.64 V to afford the overall current density of 10 mA cm⁻² (Fig. 5b), which is not only superior to those for Ni₂P NS/NF||Ni₂P NS/NF (1.69 V), NiFe-OH NS/NF||NiFe-OH NS/NF (1.73 V) and NF||NF (1.85 V), but comparable to those of reported advanced overall water splitting systems. Long-term chronopotentiometric curve for NiFe-OH NS/NF (+)||Ni₂P NS/NF (-) recorded at the constant 10 mA cm⁻² in 1.0 M KOH shows that this

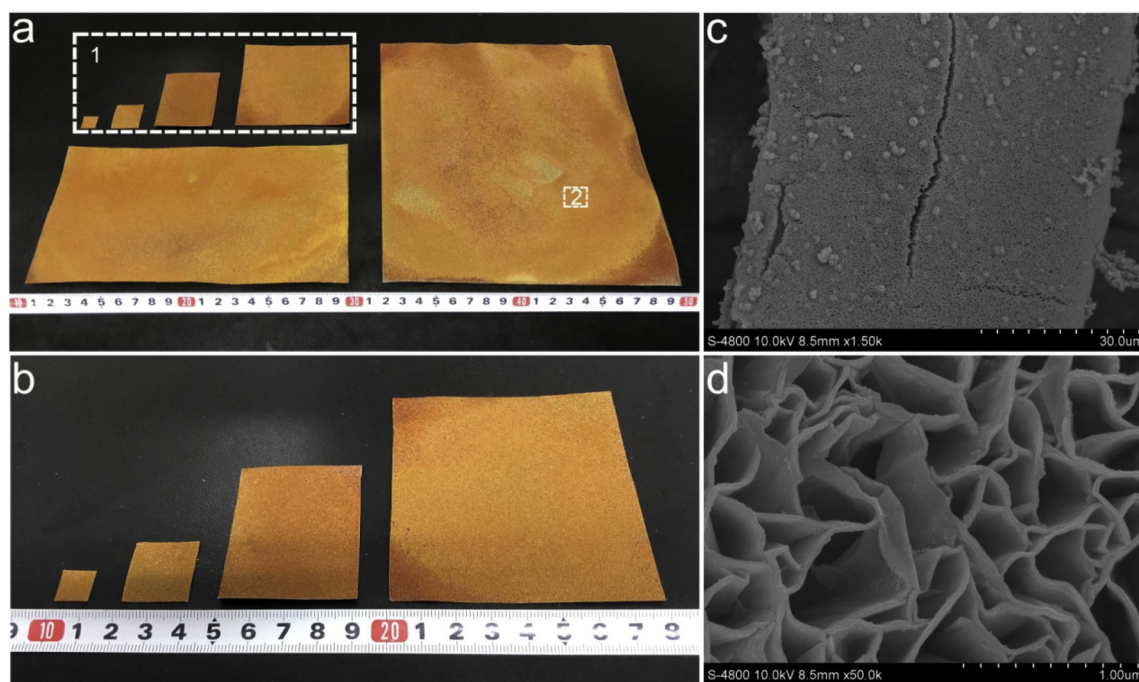


Fig. 4. Photograph and SEM image of the NiFe-OH NS/NF at different scales. (a) The photograph of different NiFe-OH NS/NF pieces synthesized at various scales. (b) Closer view of corresponding selected area (1) in a. (c) Low- and (d) high-magnification SEM images of the selected area (2) on the 20*18 cm² Ni foam substrate in a.

electrode pair could well sustain the full water splitting for at least 25 h (Fig. 5c).

We noted that such water-electrolysis device could also be powered by a simulated photosource. In this system, a NiFe-OH NS/NF anode and a Ni₂P NS/NF cathode were connected to the positive and negative terminals of a 2.0 V solar panel, respectively. In order to monitor the

voltage applied to the electrolyzer, a digital multimeter was utilized to connect in parallel to the terminals of the solar panel [60]. Fig. 5d and e shows the schematic diagram and photograph of the simulated solar energy driven water-electrolysis device, respectively, and corresponding dynamic process was recorded in a short video (Movie S1). It could be clearly observed that O₂ or H₂ bubbles generated on the

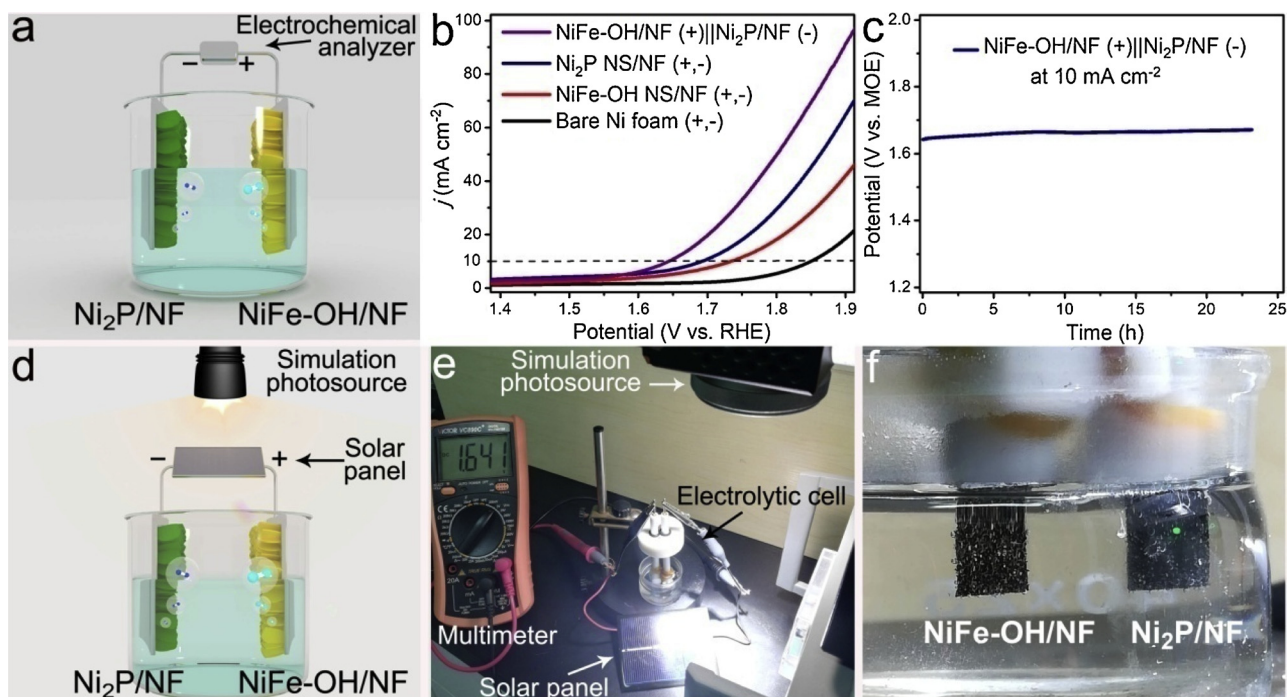


Fig. 5. Overall water-splitting devices driven by the NiFe-OH NS/NF (+)||Ni₂P NS/NF (-) pair. (a) The schematic diagram of electrochemical analyzer-driven overall water-electrolysis system consisted of Ni₂P NS/NF cathode and NiFe-OH NS/NF anode. (b) The comparison of overall water-electrolysis efficiency for NiFe-OH NS/NF (+)||Ni₂P NS/NF (-), Ni₂P NS/NF (+,-), NiFe-OH NS/NF (+,-) and Ni foam (+,-). (c) The chronopotentiometric curve for NiFe-OH NS/NF (+)||Ni₂P NS/NF (-) recorded at a constant current density of 10 mA cm⁻² in 1.0 M KOH. (d) The schematic diagram and (e) photograph of solar panel-driven overall water-splitting system consisted of Ni₂P NS/NF cathode and NiFe-OH NS/NF anode. (f) Closer view of the electrode surfaces in the solar panel-driven water-electrolysis system.

surface of both two electrodes at 1.64 V in a closer view of this system (Fig. 5f and Movie S2), indicative of the feasibility of utilizing solar energy to drive this system. Such solar energy powered overall water-splitting hybrid device has a promising prospect to be applied in portable, energy-saving and large-scale solar-to-hydrogen conversion in future distributed energy storage technologies [39,61].

4. Conclusion

In conclusion, a facile ambient redox and hydrolysis co-precipitation strategy was proposed to *in situ* fabricate well-aligned Ni-Fe hydroxide nanosheets array on Ni foam (NiFe-OH NS/NF). By precise control of the synthetic conditions like soaking time and Fe^{3+} concentration, bare Ni foam could be partially dissolved and simultaneously converted into the Ni-Fe hydroxides with tailorable chemical composition and physical morphology. The highly-oriented amorphous and nanoporous nanosheets structure as well as strong electronic interaction between Ni and Fe species endow this NiFe-OH NS/NF with excellent OER activity that current densities of 50 and 500 mA cm^{-2} could be achieved at low overpotentials of 244 and 292 mV in base, respectively. Moreover, the manufacturing and raw-materials cost to synthesize the NiFe-OH NS/NF by this strategy is estimated to be just \$0.0165 per cm^2 , much lower than those for other reported self-supported Fe-containing OER catalysts. Also, the NiFe-OH NS/NF at larger scales (e.g., $20 \times 18 \text{ cm}^2$) could be easily obtained by use of this strategy, endowing the NiFe-OH NS/NF with a higher likelihood of realizing scalable production. This novel ambient *in situ* synthetic approach not only offers us a possibility to the low-cost and large-scale production of NiFe-based anode materials for practical-oriented water oxidation, but could be easily extendable to the synthesis of other transition metal-based nanoarray monoliths for applications.

Acknowledgments

W. Zhu and T. Zhang contributed equally to this work. The authors thank the National Natural Science Foundation of China (21675127) and the Shaanxi Provincial Science Fund for Distinguished Young Scholars (2018JC-011). The authors also thank Dr. Zhengtao Luo for help with the treatment of Movies and schematic diagrams.

Appendix A. Supplementary data

Supplementary material related to this article can be found, in the online version, at doi:<https://doi.org/10.1016/j.apcatb.2018.12.021>.

References

- [1] S. Chu, A. Majumdar, *Nature* 488 (2012) 294–303.
- [2] M.S. Faber, S. Jin, *Energy Environ. Sci.* 7 (2014) 3519–3542.
- [3] M.G. Walter, E.L. Warren, J.R. McKone, S.W. Boettcher, Q. Mi, E.A. Santori, N.S. Lewis, *Chem. Rev.* 110 (2010) 6446–6473.
- [4] X. Zou, Y. Zhang, *Chem. Soc. Rev.* 44 (2015) 5148–5180.
- [5] Y. Jiao, Y. Zheng, M. Jaroniec, S.Z. Qiao, *Chem. Soc. Rev.* 44 (2015) 2060–2086.
- [6] M.S. Dresselhaus, L.L. Thomas, *Nature* 414 (2001) 332–337.
- [7] H. Zhou, F. Yu, J. Sun, R. He, S. Chen, C.-W. Chu, Z. Ren, *PNAS* 114 (2017) 5607–5611.
- [8] H. Li, Q. Li, P. Wen, T.B. Williams, S. Adhikari, C. Dun, C. Lu, D. Itanze, L. Jiang, D.L. Carroll, G.L. Donati, P.M. Lundin, Y. Qiu, S.M. Geyer, *Adv. Mater.* 30 (2018) 1705796.
- [9] J. Yin, Y. Li, F. Lv, M. Lu, K. Sun, W. Wang, L. Wang, F. Cheng, Y. Li, P. Xi, S. Guo, *Adv. Mater.* 29 (2017) 1704681.
- [10] P. Liu, D. Gao, W. Xiao, L. Ma, K. Sun, P. Xi, D. Xue, J. Wang, *Adv. Funct. Mater.* 28 (2018) 1706928.
- [11] S. Wang, J. Qin, T. Meng, M. Cao, *Nano Energy* 39 (2017) 626–638.
- [12] D. Wu, Y. Wei, X. Ren, X. Ji, Y. Liu, X. Guo, Z. Liu, A.M. Asiri, Q. Wei, X. Sun, *Adv. Mater.* 30 (2018) 1705366.
- [13] H. Zhou, F. Yu, Q. Zhu, J. Sun, F. Qin, L. Yu, J. Bao, Y. Yu, S. Chen, Z. Ren, *Energy Environ. Sci.* DOI: <https://doi.org/10.1039/C8EE00927A>.
- [14] F. Lu, M. Zhou, Y. Zhou, X. Zeng, *Small* 13 (2017) 1701931.
- [15] J. Suntivich, H.A. Gasteiger, N. Yabuuchi, H. Nakanishi, J.B. Goodenough, Y. Shao-Horn, *Nat. Chem.* 3 (2011) 546–550.
- [16] L. Han, S. Dong, E. Wang, *Adv. Mater.* 28 (2016) 9266–9291.
- [17] H. Sun, Y. Lian, C. Yang, L. Xiong, P. Qi, Q. Mu, X. Zhao, J. Guo, Z. Deng, Y. Peng, *Energy Environ. Sci.* DOI: <https://doi.org/10.1039/C8EE00934A>.
- [18] C. Zhu, A. Wang, W. Xiao, D. Chao, X. Zhang, N.H. Tiep, S. Chen, J. Kang, X. Wang, J. Ding, J. Wang, H. Zhang, H.J. Fan, *Adv. Mater.* 30 (2018) 1705516.
- [19] Y. Jin, S. Huang, X. Yue, H. Du, P.K. Shen, *ACS Catal.* 8 (2018) 2359–2363.
- [20] G. Zhang, Y. Feng, W. Lu, D. He, C. Wang, Y. Li, X. Wang, F. Cao, *ACS Catal.* 8 (2018) 5431–5441.
- [21] K. Fominykh, P. Chernev, I. Zaharieva, J. Sicklinger, G. Stefanic, A. Pokharel, S. Bocklein, C. Scheu, T. Bein, D. Fattakhova-Rohlfing, *ACS Nano* 9 (2015) 5180–5188.
- [22] Y. Li, H. Zhang, M. Jiang, Q. Zhang, P. He, X. Sun, *Adv. Funct. Mater.* 27 (2017) 1702513.
- [23] Q. Liu, L. Xie, Z. Liu, G. Du, A.M. Asiri, X. Sun, *Chem. Commun. (Camb.)* 53 (2017) 12446–12449.
- [24] Y. Zhu, W. Zhou, Y. Chen, J. Yu, M. Liu, Z. Shao, *Adv. Mater.* 27 (2015) 7150–7155.
- [25] L. Trotochaud, S.L. Young, J.K. Ranney, S.W. Boettcher, *J. Am. Chem. Soc.* 136 (2014) 6744–6753.
- [26] F. Dionigi, P. Strasser, *Adv. Energy Mater.* 6 (2016) 1600621.
- [27] M. Gong, H. Dai, *Nano Res.* 8 (2015) 23–39.
- [28] T. Wang, G. Nam, Y. Jin, X. Wang, P. Ren, M. G. Kim, J. Liang, X. Wen, H. Jang, J. Han, Y. Huang, Q. Li, J. Cho, *Adv. Mater.* DOI: <https://doi.org/10.1002/adma.201800757>.
- [29] N. Li, D.K. Bediako, R.G. Hadd, D. Hayes, T.J. Kempa, Fv. Cube, D.C. Bell, L.X. Chen, D.G. Nocera, *PNAS* 114 (2017) 1486–1491.
- [30] D. Friebe, M.W. Louie, M. Bajdich, K.E. Sanwald, Y. Cai, A.M. Wise, M.-J. Cheng, D. Sokaras, T.-C. Weng, R. Alonso-Mori, R.C. Davis, J.R. Bargar, J.K. Nørskov, A. Nilsson, A.T. Bell, *J. Am. Chem. Soc.* 137 (2015) 1305–1313.
- [31] H. Shin, H. Xiao, W.A. Goddard III, *J. Am. Chem. Soc.* 140 (2018) 6745–6748.
- [32] H. Xiao, H. Shin, W.A. Goddard III, *PNAS* 115 (2018) 5872–5877.
- [33] Q. Zhou, Y. Chen, G. Zhao, Y. Lin, Z. Yu, X. Xu, X. Wang, H.K. Liu, W. Sun, S.X. Dou, *ACS Catal.* 8 (2018) 5382–5390.
- [34] X. Lu, C. Zhao, *Nat. Commun.* 6 (2015) 6616.
- [35] G. Chen, T. Wang, J. Zhang, P. Liu, H. Sun, X. Zhuang, M. Chen, X. Feng, *Adv. Mater.* 30 (2018) 1706279.
- [36] Y. Yang, L. Dang, M.J. Shearer, H. Sheng, W. Li, J. Chen, P. Xiao, Y. Zhang, R.J. Hamers, S. Jin, *Adv. Energy Mater.* 8 (2018) 1703189.
- [37] J. Zhang, J. Liu, L. Xi, Y. Yu, N. Chen, S. Sun, W. Wang, K.M. Lange, B. Zhang, *J. Am. Chem. Soc.* 140 (2018) 3876–3879.
- [38] J. Liu, D. Zhu, T. Ling, A. Vasileff, S.-Z. Qiao, *Nano Energy* 40 (2017) 264–273.
- [39] Y. Jia, L. Zhang, G. Gao, H. Chen, B. Wang, J. Zhou, M.T. Soo, M. Hong, X. Yan, G. Qian, J. Zou, A. Du, X. Yao, *Adv. Mater.* 29 (2017) 1700017.
- [40] S. Yin, W. Tu, Y. Sheng, Y. Du, M. Kraft, A. Borgna, R. Xu, *Adv. Mater.* 30 (2018) 1705106.
- [41] L. Zhang, J. Wang, X. Ren, W. Zhang, T. Zhang, X. Liu, T. Du, T. Li, J. Wang, J. Mater. Chem. A Mater. Energy Sustain. 6 (2018) 21029–21038.
- [42] J. Zhang, T. Wang, P. Liu, Z. Liao, S. Liu, X. Zhuang, M. Chen, E. Zschech, X. Feng, *Nat. Commun.* 8 (2017) 15437.
- [43] J.-X. Feng, S.-H. Ye, H. Xu, Y.-X. Tong, G.-R. Li, *Adv. Mater.* 28 (2016) 4698–4703.
- [44] J. Deng, P. Ren, D. Deng, X. Bao, *Angew. Chem. Int. Ed.* 54 (2015) 2100–2104.
- [45] J. Liu, Y. Ji, J. Nai, X. Niu, Y. Luo, L. Guo, S. Yang, *Energy Environ. Sci.* DOI: <https://doi.org/10.1039/c8ee00611c>.
- [46] P. Cai, J. Huang, J. Chen, Z. Wen, *Angew. Chem. Int. Ed.* 56 (2017) 4858–4861.
- [47] A. Indra, P.W. Menezes, N.R. Sahraie, A. Bergmann, C. Das, M. Tallarida, D. Schmeißer, P. Strasser, M. Driess, *J. Am. Chem. Soc.* 136 (2014) 17530–17536.
- [48] H.B. Li, M.H. Yu, F.X. Wang, P. Liu, Y. Liang, J. Xiao, C.X. Wang, Y.X. Tong, G.W. Yang, *Nat. Commun.* 4 (2013) 1894.
- [49] Z. Zhao, H. Wu, H. He, X. Xu, Y. Jin, J. Mater. Chem. A Mater. Energy Sustain. 3 (2015) 7179–7186.
- [50] J.-H. Kim, D.H. Youn, K. Kawashima, J. Lin, H. Lim, C.B. Mullins, *Appl. Catal. B-Environ.* 225 (2018) 1–7.
- [51] M. Gong, Y. Li, H. Wang, Y. Liang, J.Z. Wu, J. Zhou, J. Wang, T. Regier, F. Wei, H. Dai, *J. Am. Chem. Soc.* 135 (2013) 8452–8455.
- [52] X. Wang, H. Zhang, H. Lin, S. Gupta, C. Wang, Z. Tao, H. Fu, T. Wang, J. Zheng, G. Wu, X. Li, *Nano Energy* 25 (2016) 110–119.
- [53] J. Wang, L. Ji, S. Zuo, Z. Chen, *Adv. Energy Mater.* 7 (2017) 1700107.
- [54] X.-F. Lu, D.-J. Wu, R.-Z. Li, Q. Li, S.-H. Ye, Y.-X. Tong, G.-R. Li, *J. Mater. Chem. A Mater. Energy Sustain.* 2 (2014) 4706–4713.
- [55] C. Tang, R. Zhang, W. Lu, L. He, X. Jiang, A.M. Asiri, X. Sun, *Adv. Mater.* 29 (2017) 1602441.
- [56] L. He, D. Zhou, Y. Lin, R. Ge, X. Hou, X. Sun, C. Zheng, *ACS Catal.* 8 (2018) 3859–3864.
- [57] C.C.L. McCrory, S. Jung, J.C. Peters, T.F. Jaramillo, *J. Am. Chem. Soc.* 135 (2013) 16977–16987.
- [58] P. Li, X. Duan, Y. Kuang, Y. Li, G. Zhang, W. Liu, X. Sun, *Adv. Energy Mater.* 8 (2018) 1703341.
- [59] C. Tang, R. Zhang, W. Lu, Z. Wang, D. Liu, S. Hao, G. Du, A.M. Asiri, X. Sun, *Angew. Chem. Int. Ed.* 56 (2017) 842–846.
- [60] A. Sivanantham, S. Shanmugam, *Appl. Catal. B-Environ.* 203 (2017) 485–493.
- [61] A. Sivanantham, P. Ganesan, S. Shanmugam, *Adv. Funct. Mater.* 26 (2016) 4661–4672.